Hybrid PET/MR Imaging: An Algorithm to Reduce Metal Artifacts from Dental Implants in Dixon-Based Attenuation Map Generation Using a Multiacquisition Variable-Resonance Image Combination Sequence

Irene A. Burger[1,2], Moritz C. Wurnig[1], Anton S. Becker[1], David Kenkel[1], Gaspar Delso[3], Patrick Veit-Haibach[1,2], and Andreas Boss[1]

[1]Institute of Diagnostic and Interventional Radiology, University Hospital Zurich, Zurich, Switzerland; [2]Department of Nuclear Medicine, University Hospital Zurich, Zurich, Switzerland; and [3]GE Healthcare, Waukesha, Wisconsin

It was the aim of this study to implement an algorithm modifying Dixon-based MR imaging datasets for attenuation correction in hybrid PET/MR imaging with a multiacquisition variable resonance image combination (MAVRIC) sequence to reduce metal artifacts. **Methods:** After ethics approval, in 8 oncologic patients with dental implants data were acquired in a trimodality setup with PET/CT and MR imaging. The protocol included a whole-body 3-dimensional dual gradient-echo sequence (Dixon) used for MR imaging–based PET attenuation correction and a high-resolution MAVRIC sequence, applied in the oral area compromised by dental implants. An algorithm was implemented correcting the Dixon-based μ maps using the MAVRIC in areas of Dixon signal voids. The artifact size of the corrected μ maps was compared with the uncorrected MR imaging μ maps. **Results:** The algorithm was robust in all patients. There was a significant reduction in mean artifact size of 70.5% between uncorrected and corrected μ maps from 697 ± 589 mm^2 to 202 ± 119 mm^2 ($P = 0.016$). **Conclusion:** The proposed algorithm could improve MR imaging–based attenuation correction in critical areas, when standard attenuation correction is hampered by metal artifacts, using a MAVRIC.

Key Words: MRI based attenuation correction; signal void; μ maps

J Nucl Med 2015; 56:93–97
DOI: 10.2967/jnumed.114.145862

After the first clinical hybrid PET/MR imaging system became commercially available in 2010 (*1*), fully integrated PET/MR imaging systems have increasingly been installed within the last few years (*2,3*). In contrast to a trimodality PET/CT–MR imaging setup, fully integrated PET/MR imaging scanners need a robust PET attenuation-correction (AC) algorithm based on MR imaging data. Because there is no direct relationship between MR imaging signals and the attenuation coefficient of tissue, conventional MR imaging data cannot directly be used for AC (*4*). Two main strategies have been investigated to facilitate fast and automated AC. The first approach is the use of morphology templates generated from transmission images (atlas-based techniques) (*5*). This approach has mainly been used for MR imaging/AC of brain PET but is also discussed for body PET/MR imaging. However, the high variability between patients may lead to unsatisfactory results (*6*). The second approach is based on tissue segmentation with rapid Dixon-based MR acquisition of a dual-echo 3-dimensional volumetric dataset. On the basis of the differentiation of fat and water, attenuation maps (μ maps) are generated by segmentation into 3 classes with different attenuation coefficients, background, fat, and soft tissue, or 4 classes including the lung (*7*). A comprehensive review for this segmentation method was given by Hoffmann et al. (*8*). Segmentation techniques disregard the influence of cortical bone, although a CT AC simulation study with and without bone segmentation showed that standardized uptake values of lesions within the bone or adjacent to cortical bone are significantly affected by AC without bone segmentation (*9*). Other groups suggested ultrashort-echo time (UTE) Dixon MR imaging sequences for additional bone segmentation to improve the correlation between PET data after AC with CT or MR (*10*).

However, besides the lack of bone information, all dual-echo gradient-echo pulse sequences used for Dixon imaging are highly affected by dephasing artifacts in areas of magnetic field inhomogeneities causing large signal voids (e.g., due to arthroplasty or dental implants). These signal voids can lead to substantial underestimation of ^{18}F-FDG uptake within the area of artifact (*11*). Atlas-based AC has been suggested to compensate for these artifacts (*11*); however, this technique depends on a substantial amount of a priori knowledge of the anatomy and requires sophisticated computer hardware because of its computation requirements (*11*).

Not only is AC affected by metal implants, but also diagnostic accuracy is strongly degraded by susceptibility artifacts in conventional spin-echo and gradient-echo sequences (*12*). To overcome this general limitation of MR imaging, dedicated MR sequences have been developed, which are able to compensate for metal artifacts to a large extent. Multiacquisition variable-resonance image combination (MAVRIC) and the slice encoding for metal artifact correction technique have shown promising results in reducing susceptibility artifacts in arthroplasty imaging (*13–16*). MAVRIC and slice encoding for metal artifact correction are too time-consuming for MR acquisition covering large body areas; however, they are well suited for dedicated application in areas affected by

Received Jul. 19, 2014; revision accepted Nov. 13, 2014.
For correspondence or reprints contact: Irene Burger, Nuclear Medicine, University Hospital Zurich, Ramistrasse 100, CH-8091 Zurich, Switzerland.
E-mail: irene.burger@usz.ch
Published online Dec. 11, 2014.

metal artifacts, for example, for imaging of the oral cavity in patients with head and neck tumors in the presence of dental implants.

The aim of this investigation was to develop and implement an algorithm that uses a diagnostic MAVRIC dataset to correct Dixon-based μ maps in the areas of signal voids due to dental implants and to test it in oncologic patients examined in a trimodality PET/CT–MR imaging system to compare μ maps derived from the new algorithm with conventional Dixon-based μ maps and CT-based μ maps as a clinical reference standard.

MATERIALS AND METHODS

Subjects

This is a retrospective analysis of a prospective study with patients referred for ^{18}F-FDG PET/CT who gave written informed consent for an additional MR imaging scan during the ^{18}F-FDG uptake time to obtain a PET/CT/MR imaging study. All measurements were conducted with the approval of the local ethics committee. Eight consecutive patients were selected who had dental implants and were scanned in December 2013 through January 2014 (5 male and 3 female patients). Examinations were performed using a sequential trimodality PET/CT–MR imaging system consisting of a Discovery 750w 3T MR imaging scanner (GE Healthcare) and a Discovery 690 PET/CT scanner (GE Healthcare). A shuttle device enabling the transfer of the patient table from the MR imager to the PET/CT imager without changing the patient's position was used. Standard PET/CT was acquired, and axial images of the oral cavity were obtained from low-dose CT (120 kV, tube current with automated dose modulation with 60–440 mA/slice). PET data were acquired in 3-dimensional time-of-flight mode, with a scan duration of 2 min per bed position.

In the MR imaging acquisition protocol, a transverse (axial) dual-echo 3-dimensional encoded gradient-echo pulse sequence was used (liver acquisition with volume acceleration; repetition time, 4.3 ms; echo time, 1.3 and 2.6 ms; matrix size, 512 × 512 × 152; spatial resolution, 0.98 × 0.98 × 2.0 mm; transversal field of view, 50 × 50 cm; bandwidth, 142.86 KHz; parallel imaging acceleration factor, 2; total acquisition time, 14 s) for generation of MR-based μ maps (*9*). In the area of dental implants, a transversal 3-dimensional encoded MAVRIC (MAVRIC SL; GE Healthcare) sequence was applied (repetition time, 4,000 ms; echo time, 7.6 ms; 24 spectral bins of 2.25 kHz each to cover ±11 kHz; matrix size, 384 × 256; in-plane resolution, 0.47 × 0.47 mm; slice thickness, 3 mm; 24 slices; phase acceleration, 2), with a total acquisition time of 6:38 min. The MAVRIC sequence was used both for diagnostic imaging and to calculate the corrected μ maps.

Correction Algorithm

The following semiautomatic algorithm was developed and tested in the programming language Matlab (The MathWorks). A flow chart of the algorithm is provided in Figure 1. At the beginning, the DICOM datasets from the Dixon and the MAVRIC sequences are loaded and coregistered using a Matlab code for rigid image alignment. Then the user has to determine 2 parameters manually by drawing regions of interest in the respective images: the mean value of the noise in the background area of the Dixon sequence and the mean value of the noise in the background of the MAVRIC sequence. From a histogram analysis, the peak of the soft-tissue signal in the Dixon water dataset and the peak of the fat signal of the Dixon fat dataset are determined (Matlab histc and counts functions). The mean fat signal of the MAVRIC sequence is calculated from a coregistration to the Dixon fat dataset (coregistration technique described below). Later in the algorithm, these 5 manually or automatically determined parameters are required for segmentation using thresholds and automatic replacement of pixel values.

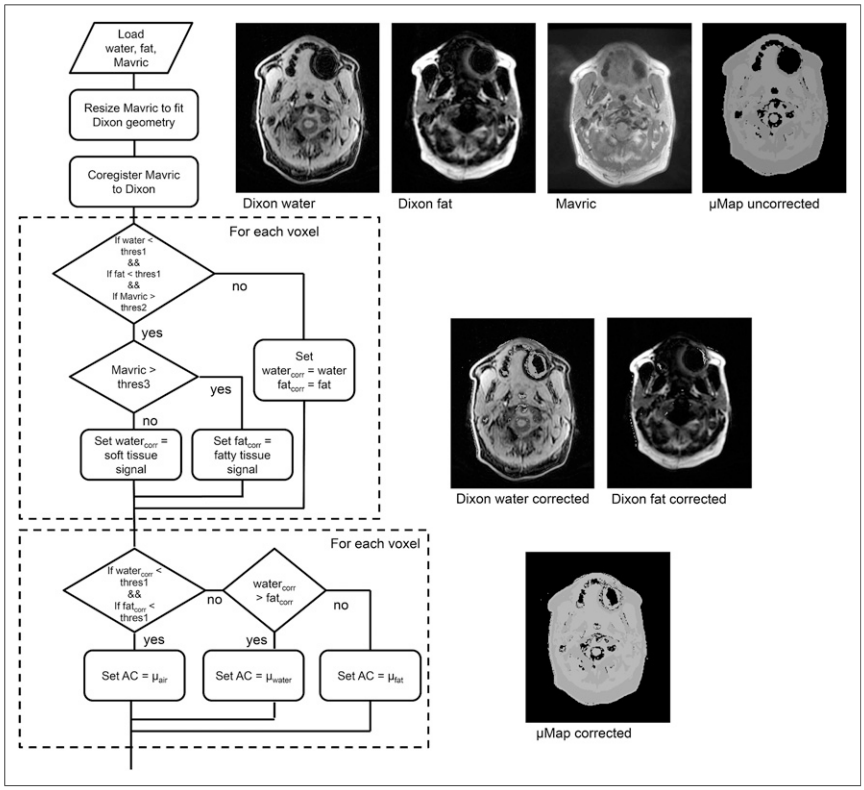

FIGURE 1. Flow chart of proposed algorithm is depicted on left side. On right side, typical images and corresponding modifications during execution of algorithm are demonstrated. thres = threshold; water = Dixon water; fat = Dixon fat.

Because the MAVRIC sequence was acquired only over the oral cavity compromised with metal artifact, the field of view was chosen manually and did not correspond to the Dixon field of view. In a first computation step, the MAVRIC dataset is interpolated and resized to fit the geometry of the Dixon sequence. Then for each Dixon slice overlapping with the MAVRIC dataset, the best corresponding slice position in the MAVRIC stack is determined. This MAVRIC slice is coregistered to the corresponding Dixon slice using the function findoff written by Davide di Gloria, accessible via Matlab Central file exchange (http://www.mathworks.ch/matlabcentral/fileexchange).

After coregistration, the following steps were performed for each voxel in a first loop: if the signals in the Dixon water and fat sequence were both on the order of the noise level (below threshold 1) and the MAVRIC sequence exhibited tissue signal (above threshold 2), the algorithm assumed that this voxel belonged to a signal void due to a metal artifact. Then the algorithm looked up whether the signal of the voxel in the MAVRIC sequence was higher than a threshold separating water and fat (threshold 3). If the signal was below threshold 3, soft tissue was assumed, and in the Dixon water sequence the voxel was set to soft-tissue signal. If the signal intensity was above threshold 3, adipose tissue was assumed and the respective voxel in the Dixon fat sequence was set to the value of the fat signal.

In a second loop, the modified Dixon water and fat datasets were used for segmentation of air, soft tissue, and adipose tissue, thereby generating the corresponding μ map as previously described (*9*). For each voxel exhibiting signal above the noise level in either the Dixon fat or the water dataset, the attenuation coefficient of soft tissue (0.10 cm^{-1}) or adipose tissue (0.09 cm^{-1}) was set in the μ map, depending on the dominant signal of the water and fat datasets. For voxels with signal in the area of the noise level (below threshold 1), the attenuation coefficient was set to 0, corresponding to air.

After implementation, the algorithm was optimized to generate plausible and robust μ maps. Therefore, 3 thresholds had to be determined: threshold 1, corresponding to the upper threshold of the noise level in the Dixon sequence (every signal below threshold 1 was rated as noise); threshold 2, determining soft-tissue signal in the MAVRIC sequence (every signal above threshold 2 was rated as soft tissue); and threshold 3 in the MAVRIC sequence, separating soft tissue and adipose tissue signal with higher values for fat signal. The thresholds were optimized by visual control in 3 patients to achieve an optimal tradeoff with limited artifacts and a robust and high signal.

For comparison, μ maps were also generated from the uncorrected Dixon sequence using the above-described second loop. CT-based μ maps were calculated using a conventionally applied bilinear transformation of the attenuation coefficient of the low-dose CT dataset (*17*).

Quantitative and Qualitative Analysis

The running time of the algorithm (between the start of reading of the image data and the end of generation of the μ maps including the time needed for drawing of the required regions of interest) was measured for each subject. Furthermore, the signal void was quantitatively assessed for each metal artifact using the freely available open-source software GIMP, version 2.8.2. On the axial images of corrected and uncorrected μ maps, the largest diameter a_1 and the corresponding orthogonal diameter a_2 were measured. The area of the artifact was calculated by assuming the shape of the artifact to be ellipsoidal, using the equation $A = \pi \times (a_1/2) \times (a_2/2)$.

The images were qualitatively assessed independently by 2 interpreters with a score from 1 to 4: 1, severe artifacts, nonuseable μ map; 2, some artifacts, μ map barely usable; 3, few artifacts, μ map usable; and 4 = barely visible or no artifacts, μ map well usable.

Statistics

First, a normal distribution of the assessed parameters was ensured with the Kolmogorov–Smirnov test. Consecutive means and SDs were computed. Then means of the size of the observed artifacts in the uncorrected and the corrected MR imaging μ map were compared using a 1-sided paired *t* test. To compare differences in the interpreter scores between interpreters and the different μ maps, a repeated-measurement ANOVA was computed. For significant effects, a post hoc analysis using a Bonferroni adjustment was performed. Furthermore interinterpreter agreement was assessed using the intraclass correlation coefficient. All *P* values less than 0.05 were considered to be statistically significant. All statistical analyses were performed using commercially available software (GraphPad Prism, version 5.04 [GraphPad Software], and SPSS Statistics, version 22.0.0.1 [IBM]) for Windows (Microsoft).

RESULTS

The algorithm was successfully applied in all patients, with resulting computation of corrected Dixon water and fat datasets and corrected μ maps (Figs. 1 and 2).

Optimal thresholds for tissue and artifact segmentation were determined: the optimal setting of threshold 1 was determined as 10 times the mean noise level in the background of the Dixon image. The optimal level of threshold 2 was determined as 2.5 times the mean noise level in the background of the MAVRIC sequence. And the optimal setting of threshold 3 was found to be 50% of the mean signal intensity of adipose tissue in the MAVRIC sequence.

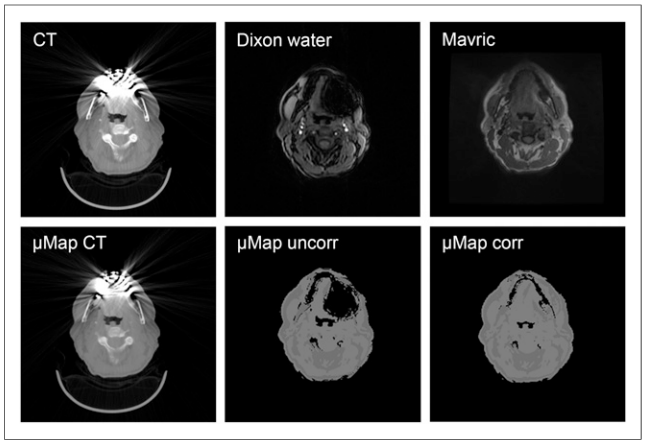

FIGURE 2. (Top) Typical examples of images obtained from low-dose CT, water dataset of Dixon sequence, and MAVRIC sequence are shown. (Bottom) Corresponding μ maps generated from CT, Dixon sequence alone, and new correction algorithm are shown.

Running time of the algorithm including the user interaction was short and showed little variation between the different subjects, with a mean of 78 ± 5 s.

The conventional μ map generated with the Dixon sequence alone exhibited a mean area of the signal void of 697.6 ± 588.7 mm^2. When the correction algorithm with the additional information of the MAVRIC sequence was used, the artifact size reduced significantly to 202.8 ± 119.2 mm^2 ($P = 0.016$) (Table 1; Figs. 2 and 3), corresponding to a mean reduction of the artifact size by 70.5%.

ANOVA analysis revealed no significant differences between the evaluation of the 2 interpreters regarding the artifacts present in the computed μ maps ($P = 0.410$). Intraclass correlation coefficient values for artifact assessment were 0.48 for corrected MR imaging μ maps, 0.60 for uncorrected MR imaging μ maps, and 0.56 for the CT μ maps, indicating a fair to good agreement corresponding to Cicchetti (*18*). However, the observed artifacts varied statistically significantly between the corrected MR imaging μ maps (mean score, 2.94 ± 0.77) and the uncorrected MR imaging μ maps (mean score, 2.06 ± 0.68, $P = 0.001$), whereas the CT μ maps (mean score, 1.69 ± 0.87) were slightly worse than uncorrected MR imaging μ maps ($P = 0.912$).

DISCUSSION

Dental artifacts can cause substantial overestimation of ^{18}F-FDG uptake due to artifacts in the CT-based μ map. This overestimation can be avoided with the proposed algorithm, with a significant reduction in ^{18}F-FDG uptake overestimation within the oral cavity (*19*). With MR-based AC, however, it is known that large signal voids due to metal artifacts can cause substantial underestimation of ^{18}F-FDG uptake (*20*). Therefore, a reduction of signal voids in the area of interest is mandatory for the accurate assessment of tumor metabolism.

Dixon-based AC has several advantages: because of a short repetition time, a fast whole-body 3-dimensional dataset can be

TABLE 1
Artifact Size

Measurements	Mean ± SD (mm^2)	Median (mm^2)	Range (mm^2)
Area size of uncorrected artifacts	697.6 ± 588.7	561.7	144.6–2012
Area size of corrected artifacts	202.8 ± 119.2	203.8	53.2–380.7
Difference	494.8 ± 523.6*	310.8	91.4–1631.3

*$P = 0.016$.

acquired that allows the segmentation of water and fat for different attenuation coefficients (0.10 and 0.09 cm^{-1}). Furthermore, Dixon-based AC is fast and robust (*21*). Dixon dual-echo gradient-echo pulse sequences might moreover be suitable for lung imaging, because in the detection rate of small pulmonary nodules, there was no statistically significant difference on a patient-based evaluation, compared with low-dose CT (*22*). For AC, however, the Dixon-based μ maps have 2 major disadvantages: first, bone cannot be distinguished from air; therefore, no accurate bone segmentation is possible. Second, the dual-echo gradient-echo pulse sequences, as all gradient-echo sequences, are especially susceptible to magnetic field distortions arising from metal implants as opposed to spin-echo sequences because the transverse magnetization is not refocused by a 180° refocusing pulse. However, spin-echo sequences are not suitable for the computation of whole-body μ maps because these sequences require relatively long acquisition times and can result in perceptible tissue warming caused by the deposition of a large amount of radiofrequency energy.

In the present investigation, we were able to show that the newly proposed algorithm may be used to significantly improve μ maps derived by tissue segmentation of Dixon MR imaging datasets. The algorithm resulted in a 70% reduction of the area of the signal-dephasing artifact in patients with dental implants in the oral cavity. Visual assessment of the μ map quality demonstrated superior image quality of the corrected MR imaging μ maps not only when compared with uncorrected Dixon-based μ maps but also when compared with the μ map generated from low-dose CT using a commonly applied bilinear transformation algorithm. The algorithm uses a MAVRIC sequence, which could be implemented in a diagnostic imaging protocol in the area of interest to improve the diagnostic accuracy in the presence of metal artifacts. Therefore, if artifacts are present, an additional sequence dedicated to the AC only is not required, because MAVRIC could be used for both diagnostic image analysis and AC. Moreover, the algorithm requires only little computation power and user interaction, providing the corrected μ map within less than 1.5 min after processing time.

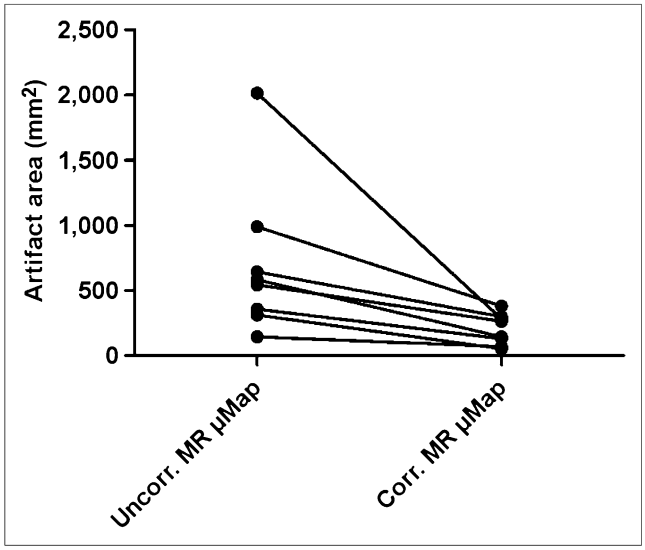

FIGURE 3. Size of metal artifacts in μ maps decreased in all assessed subjects. Mean artifact size decreased from 697.6 mm^2 in uncorrected MR imaging μ map to 202.8 mm^2 in corrected MR imaging μ map ($P = 0.016$), corresponding to mean reduction of 70%. Corr. = corrected; Uncorr. = uncorrected.

For PET/MR in oropharyngeal cancer, a diagnostic sequence with high image resolution and good soft-tissue contrast of the oral cavity is mandatory for accurate tumor staging. In patients with dental implants, conventional sequences are hampered by image distortions and intravoxel signal dephasing due to a large frequency dispersion of the excited spins. This image degradation can be significantly reduced by the use of sequences capable of acquiring signal in areas of magnetic field inhomogeneities such as MAVRIC. With the presented algorithm, the same sequence for anatomic analysis can also be used to improve the Dixon-based μ map; therefore, no additional scan exclusively for AC is needed. Currently, this algorithm is implemented in the programming language Matlab on an offline computer; however, it could easily be implemented into a standard workflow running within the PET/MR scanner hardware. Because both datasets are transversally oriented, the coregistration of the datasets is easy to perform with only translation modifications. Therefore, even in the interpreter language Matlab the algorithm was able to finish within less than 1.5 min of computation time using a standard personal computer.

Alternative MR imaging sequences such as a UTE data acquisition (*23*) or even the combination of UTE with MAVRIC (*24*) have been suggested for improved AC in PET/MR imaging. The main advantage of a UTE sequence would be the detection of signal from bone, thereby facilitating bone segmentation in MR imaging–based AC. Furthermore, the short echo time results in a decreased intravoxel spin dephasing and, therefore, in reduced susceptibility artifacts due to magnetic field inhomogeneity. These advantages could be further improved if images were obtained with UTE at different spectral frequencies (UTE MAVRIC), with a significant reduction of artifacts near arthroplasty implants, however, at the cost of a long acquisition time (17 min) per field of view (*24*). The long acquisition time limits the use of UTE sequences for whole-body AC in standard workflow. Furthermore, UTE sequences cannot be used for diagnostic purposes because of the low spatial resolution and the proton density contrast only. Therefore, additional diagnostic high-resolution sequences would be needed such as a diagnostic MAVRIC sequence in the area

of dental implants. An acquisition time of 6 min still limits the use of MAVRIC for integration in PET/MR systems. Further investigations to reduce the acquisition time for MAVRIC sequences are needed for routine integration of MAVRIC in head and neck protocols in PET/MR.

Besides these direct segmentation approaches (based on Dixon or UTE sequences), another common approach for PET/MR AC is the use of an atlas-based generation of μ maps. The presented algorithm and the resulting modified Dixon images might also improve the performance of these atlas-based methods because more accurate information can be used as input.

Our study has several limitations. First, we applied the algorithm only in the area of the oral cavity and did not apply it for other regions; however, the algorithm may by applied equally well in the pelvis or other areas of metal implants. Furthermore, the last step of a complete PET reconstruction was not performed because these data were not acquired in a fully integrated PET/MR imaging system but within a trimodality PET/CT–MR imaging setup to obtain CT data as well. However, other studies have shown that large signal voids in MR imaging sequences used for AC can lead to substantial artifacts in PET reconstructions. Furthermore, it is difficult to compare MR imaging–based AC with CT-based AC given that attenuation maps are more accurate in the areas surrounding the dental implants in the former case whereas they are better around bone tissue and sinuses in the latter. It may be assumed without complete execution of the PET reconstruction that better μ maps result also in better and more accurate PET reconstructions. Another limitation arises from the form of the artifact present in the Dixon images: because of the magnetic field inhomogeneity, the Dixon sequence classifies signal close to the edge of the artifact as mainly coming from fatty tissue, resulting in a small fat ring present in the final corrected μ maps. Still, the presented algorithm provides a significant improvement over the uncorrected μ maps because significantly less tissue is wrongly classified as air.

CONCLUSION

We showed that a semiautomatic algorithm using a MAVRIC sequence can be used to correct Dixon-based μ maps, with a substantial reduction of the artifact size. This algorithm could easily be integrated into clinical workflow, requiring little additional postprocessing time and no additional scan time to improve MR imaging–AC.

DISCLOSURE

The costs of publication of this article were defrayed in part by the payment of page charges. Therefore, and solely to indicate this fact, this article is hereby marked "advertisement" in accordance with 18 USC section 1734. Gaspar Delso and Miguel Porto are employed by GE Healthcare. No other potential conflict of interest relevant to this article was reported.

ACKNOWLEDGMENTS

We thank the technologists and the administrative staff at the University Hospital of Zurich and University for their help in acquiring the data and freeing up resources.

REFERENCES

1. Delso G, Furst S, Jakoby B, et al. Performance measurements of the Siemens mMR integrated whole-body PET/MR scanner. *J Nucl Med.* 2011;52:1914–1922.
2. Catana C, Drzezga A, Heiss WD, Rosen BR. PET/MRI for neurologic applications. *J Nucl Med.* 2012;53:1916–1925.
3. Ratib O, Beyer T. Whole-body hybrid PET/MRI: ready for clinical use? *Eur J Nucl Med Mol Imaging.* 2011;38:992–995.
4. Keereman V, Mollet P, Berker Y, Schulz V, Vandenberghe S. Challenges and current methods for attenuation correction in PET/MR. *MAGMA.* 2013;26:81–98.
5. Montandon ML, Zaidi H. Atlas-guided non-uniform attenuation correction in cerebral 3D PET imaging. *Neuroimage.* 2005;25:278–286.
6. Zaidi H. Is MR-guided attenuation correction a viable option for dual-modality PET/MR imaging? *Radiology.* 2007;244:639–642.
7. Martinez-Möller A, Souvatzoglou M, Delso G, et al. Tissue classification as a potential approach for attenuation correction in whole-body PET/MRI: evaluation with PET/CT data. *J Nucl Med.* 2009;50:520–526.
8. Hofmann M, Pichler B, Scholkopf B, Beyer T. Towards quantitative PET/MRI: a review of MR-based attenuation correction techniques. *Eur J Nucl Med Mol Imaging.* 2009;36(suppl 1):S93–S104.
9. Samarin A, Burger C, Wollenweber SD, et al. PET/MR imaging of bone lesions: implications for PET quantification from imperfect attenuation correction. *Eur J Nucl Med Mol Imaging.* 2012;39:1154–1160.
10. Berker Y, Franke J, Salomon A, et al. MRI-based attenuation correction for hybrid PET/MRI systems: a 4-class tissue segmentation technique using a combined ultrashort-echo-time/Dixon MRI sequence. *J Nucl Med.* 2012;53:796–804.
11. Bezrukov I, Schmidt H, Mantlik F, et al. MR-based attenuation correction methods for improved PET quantification in lesions within bone and susceptibility artifact regions. *J Nucl Med.* 2013;54:1768–1774.
12. Schenck JF. The role of magnetic susceptibility in magnetic resonance imaging: MRI magnetic compatibility of the first and second kinds. *Med Phys.* 1996;23:815–850.
13. Chen CA, Chen W, Goodman SB, et al. New MR imaging methods for metallic implants in the knee: artifact correction and clinical impact. *J Magn Reson Imaging.* 2011;33:1121–1127.
14. Hayter CL, Koff MF, Shah P, Koch KM, Miller TT, Potter HG. MRI after arthroplasty: comparison of MAVRIC and conventional fast spin-echo techniques. *AJR.* 2011;197:W405–W411.
15. Sutter R, Hodek R, Fucentese SF, Nittka M, Pfirrmann CW. Total knee arthroplasty MRI featuring slice-encoding for metal artifact correction: reduction of artifacts for STIR and proton density-weighted sequences. *AJR.* 2013;201:1315–1324.
16. Sutter R, Ulbrich EJ, Jellus V, Nittka M, Pfirrmann CW. Reduction of metal artifacts in patients with total hip arthroplasty with slice-encoding metal artifact correction and view-angle tilting MR imaging. *Radiology.* 2012;265:204–214.
17. Burger C, Goerres G, Schoenes S, Buck A, Lonn AH, Von Schulthess GK. PET attenuation coefficients from CT images: experimental evaluation of the transformation of CT into PET 511-keV attenuation coefficients. *Eur J Nucl Med Mol Imaging.* 2002;29:922–927.
18. Cicchetti DV. Guidelines, criteria, and rules of thumb for evaluating normed and standardized assessment instruments in psychology. *Psychol Assess.* 1994;6:284–290.
19. Delso G, Wollenweber S, Lonn A, Wiesinger F, Veit-Haibach P. MR-driven metal artifact reduction in PET/CT. *Phys Med Biol.* 2013;58:2267–2280.
20. Keller SH, Holm S, Hansen AE, et al. Image artifacts from MR-based attenuation correction in clinical, whole-body PET/MRI. *MAGMA.* 2013;26:173–181.
21. Eiber M, Martinez-Moller A, Souvatzoglou M, et al. Value of a Dixon-based MR/PET attenuation correction sequence for the localization and evaluation of PET-positive lesions. *Eur J Nucl Med Mol Imaging.* 2011;38:1691–1701.
22. Stolzmann P, Veit-Haibach P, Chuck N, et al. Detection rate, location, and size of pulmonary nodules in trimodality PET/CT-MR: comparison of low-dose CT and Dixon-based MR imaging. *Invest Radiol.* 2013;48:241–246.
23. Delso G, Carl M, Wiesinger F, et al. Anatomic evaluation of 3-dimensional ultrashort-echo-time bone maps for PET/MR attenuation correction. *J Nucl Med.* 2014;55:780–785.
24. Carl M, Koch K, Du J. MR imaging near metal with undersampled 3D radial UTE-MAVRIC sequences. *Mag Reson Med.* 2013;69:27–36.